Catalytic Enhancement of Inductively Heated Fe₃O₄ Nanoparticles via Removal of Surface Ligands

Natalia S. Moura, [a] Khashayar R. Bajgiran, [a] Cameron L. Roman, [a] Luke Daemen, [b] Yongqiang Cheng, [b] Jimmy Lawrence, [a] Adam T. Melvin, [a] Kerry M. Dooley, [a] James A. Dorman*[a]

[a] N. S. Moura, K.R. Bajgiran, C. Roman, Dr. J. Lawrence, Dr. A. Melvin, Dr. K. Dooley, Dr. J. Dorman. Department of Chemical Engineering Louisiana State University 3307 Patrick F. Taylor Hall, Baton Rouge, LA 70803, USA

E-mail: jamesdorman@lsu.edu
[b] Dr. L. Daemen, Dr. Y. Cheng
Spallation Neutron Source
Oak Ridge National Lab

PO. Box 2008, Oak Ridge, TN 37831, USA

Supporting information for this article is given via a link at the end of the document.

Abstract: Heat management in catalysis is limited by each material's heat transfer efficiencies, resulting in energy losses despite current thermal engineering strategies. In contrast, induction heating of magnetic nanoparticles (NPs) generates heat at the surface of the catalyst where the reaction occurs, reducing waste heat via dissipation. However, the synthesis of magnetic NPs with optimal heat generation requires interfacial ligands, such as oleic acid, which act as heat sinks. Surface treatments using tetramethylammonium hydroxide (TMAOH) or pyridine are used to remove these ligands before applications in hydrophilic media. Herein, Fe₃O₄ NPs are surface treated to study the effect of induction heating on the catalytic oxidation of 1-octanol. While TMAOH was unsuccessful in removing oleic acid, pyridine treatment resulted in a ~2.5x increase in heat generation and product yield. Therefore, efficient surfactant removal has profound implications in induction heating catalysis.

Introduction

Heat management in catalytic processes is essential to the success of industrial operations, where the potential for energy savings was estimated to be 25% in 2015^[1], and with up to 30% energy loss as waste heat.[2] In 2010, over 80% of chemical processes involved catalysts, resulting in a total value of fuel and chemicals of \$900 billion.[3] There is a continuing motivation to utilize technologies that reduce heat dissipation and improve energy transfer to reduce the 50% energy losses which occur with thermal heating.^[4] With the rapid depletion of the U.S. energy resources coupled to population growth, catalytic industrial processes energy utilization must be improved to sustain the production of goods and our quality of life. Among the emerging areas in catalysis offering targeted heat delivery is induction heating, where magnetic materials placed in high frequency alternating magnetic fields (AMF) generate heat locally. [4a] This in situ heat generation has the added advantages of reducing risks associated with high-temperature reactor setups, shorter warming times, and power transmissions that are 1500x higher than conduction. [4a, 5] This technology also contributes to the sustainability of manufacturing processes, where induction heating replaces fuel-fired furnaces, reducing CO₂ emissions and air pollution. [6] Furthermore, these heating mechanisms are electric-based and can utilize renewable energy as its source, decreasing our dependence of fossil fuels.

The enhanced energy transfer of induction heating enables advancements in process efficiency to be implemented as a first step, and further improvements in catalyst performance can be achieved by adding active species, metal clusters, or functionalizing the surface of the NPs. [5c, 5d, 7] However, coupling magnetic heating with catalytically active materials is challenging due to the synthetic methods needed to control surface morphology, colloidal anisotropy, reduce polydispersity, and improve crystallinity. These parameters are crucial to maximize heat generation for a given nanoparticle size.[8] For example, earth-abundant Fe_3O_4 NPs, synthesized decomposition[8a, 9-10] frequently used for magnetic hyperthermia^[9], have optimum heat generation with particle diameters around 20 nm, but their catalytic properties have yet to be explored when heated magnetically. For the dual purpose of catalysis and heat generation, smaller sizes are also preferred to improve catalyst surface area. While thermal decomposition can control particle monodispersity and size, it requires bulky and long capping ligands such as oleic acid (OA).[11] The strong adsorption energies of these surfactants are known to hinder simple catalytic processes, such as the Fenton reaction.[12] Accordingly, the design of the interfacial structure for catalytic active colloids directly influences the heat transfer, requiring the removal of the persistent OA ligand shell to improve gas adsorption and limit poisoning^[12a] or coking^[13] of the Fe₃O₄ surface. This is especially relevant in induction heating, where the surfactant layer is directly attached to the heat source, which may act as a heat sink[11a] and lead to rapid coking. Current surface treatments for catalysis integration[14] involve passivation/functionalization with a solid shell or another ligand to act as a repository for the active sites, leaving the Fe₃O₄ core to direct the heat generation in the entire NP. [5c, 5d, 7a, 15] However, the presence of an organic or inorganic shell layer decreases the overall heat transfer to the reactants, and itself can interfere with the reaction.[4a] Additionally, alternative treatments (e.g., heat, UV-ozone irradiation, electrochemistry, etc.) are damaging to the Fe₃O₄ structure, resulting in a more oxidized and less magnetic γ-Fe₂O₃ phase. [12c,

Inspired by the successful ligand removal in quantum dots and semiconductors, this work aims to elucidate the relationship between heat generation and the subsequent surface chemistries by controlling the extent of OA removal using two treatments, tetramethylammonium hydroxide (TMAOH)[17] and pyridine.[18] To quantify this relationship, the catalytic oxidation of 1-octanol to 1octanal was chosen as a proof-of-concept reaction for direct comparison with literature. [19] The reaction is shown to generate aldehydes over metal oxide surfaces at ~100 °C and ketones at temperatures >350 °C in the presence of hydroxyl groups. With that in mind, TMAOH treatment was chosen as a way to add hydroxyl groups to the catalyst surface^[17, 20], thereby changing catalyst selectivity when compared to a "bare" Fe₃O₄ surface treated with pyridine. [18a, 18c] These surface treatments have already been reported to displace certain native ligands and increase hydrophilicity.[17, 21]

The detection of these surface ligands on Fe₃O₄ NPs has proven a significant challenge due to the oxide's optical and magnetic properties preventing optical/IR and magnetic (NMR) surface characterization techniques. [21b, 22] Since sensitive surface characterization is critical to understand the available surface sites and heat transfer, alternative characterization methods, such as Inelastic Neutron Scattering (INS) are necessary. INS provides a complete vibrational spectrum of surface ligands based on its high specificity for hydrogen atoms arising from differences in total scattering cross-sections (11.62 barn for Fe compared to 82.02 barn for ¹H). [23] This results in a flatter background absorbance for Fe₃O₄ than in Fourier Transform Infrared Spectroscopy (FTIR), [23d] and is employed to improve the detection of residual OA ligands.

In this work, the catalytic conversion of 1-octanol to octanal is studied using Fe₃O₄ catalysts to determine the effectiveness of induction heating. Controlled synthesis of colloidal NPs is performed to maximize magnetic-to-thermal energy conversion and achieve high surface areas. The NP surface (FTIR, INS, Thermal Gravimetric Analysis (TGA), and Brunauer-Emmett-Teller (BET) surface area) and its electronic (X-ray Photoelectron Spectroscopy (XPS)) structure were characterized in order to understand the relationship between catalytic activity and surface treatments. Previous reports have indicated successful ligand removal of Fe₃O₄. [17, 22d, 22e, 24] Herein, it was observed that TMAOH functionalized the OA layer with hydroxyl groups, not the NP surface. In contrast, pyridine surface treatments resulted in significant improvements in catalytic conversion and heat generation, allowing for the application of these NPs to similar reactions where lower temperatures can be beneficial.

Results and Discussion

Fe₃O₄ nanoparticles (NPs) were synthesized via thermal decomposition using OA and subsequently treated with TMAOH and pyridine for the catalytic oxidation of 1-octanol. The assynthesized NPs can be indexed to spinel Fe₃O₄ (magnetite *Fd-3m* space group)^[25] (Figure 1a) of ~17 nm in diameter, which is expected to have high magnetic-to-thermal heat conversion.^[11b, 26] Additionally, the co-precipitated samples and nanocubes synthesized for surface chemistry comparison, where the NPs

have no surfactants and oleate ligands (OL), respectively, were indexed to the same crystalline phase (Figure S3). No considerable changes in the size of the NPs were observed after the phase transfer treatments were performed to remove the capping agents (Figure S4). Additionally, no significant changes in morphology were observed between the as-synthesized (Figure 1b) and the TMAOH-treated NPs (Figure 1c), whereas the pyridine treatment resulted in a slight increase in agglomeration (Figure 1d). The NPs were dispersible in 1-octanol after both phase transfer treatments and exposed to the RF fields or thermal heating (200 °C) for 6 h in a sealed ampule to prevent the evaporation of the liquid. The gentle surface treatment allowed for further heterogeneous alcohol oxidation studies thermally and inductively without compromising the magnetic-to-heat conversion.

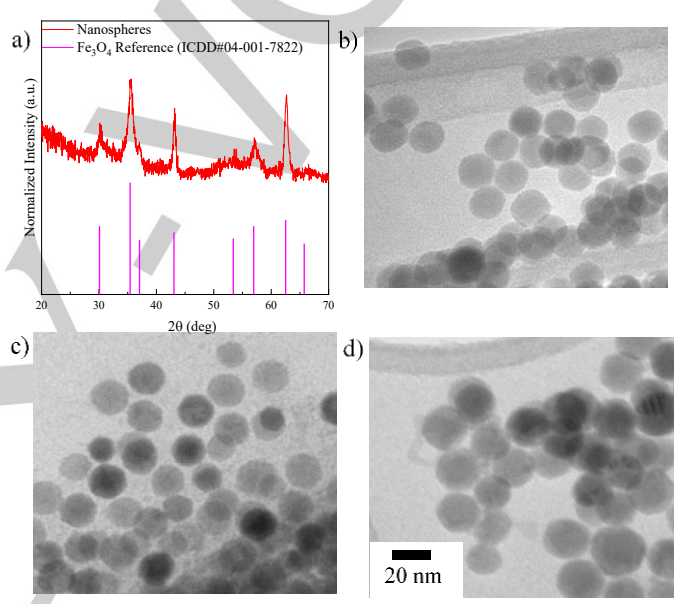


Figure 1. a) XRD of the as-synthesized nanospheres indexed to the magnetite (Fe₃O₄) crystal phase. TEM image of b) as-synthesized, c) TMAOH treated, and d) pyridine treated samples showing no significant change in morphology or size.

The catalytic performance of the synthesized NPs was compared to commercially available Fe₃O₄ (40-180 nm, VWR) powders, co-precipitated NPs and a control test using the octanol solution without catalysts (Table 1). In general, the thermal heating resulted in lower conversions of 1-octanol regardless of the method of phase transfer, with a 2.5x increase in conversion for the pyridine sample. Almost all catalytic samples from induction heating reactions improved heat transfer, which was translated into higher product yields. The pyridine treated samples outperform as-synthesized NPs thermally and inductively, increasing aldehyde yield by 4x, and demonstrating the benefits of removing capping ligands in induction heating catalysis (Table 1). Further improvements in conversion could likely be achieved using traditional promoters, solvents, and highpressure systems but are beyond the scope of this work. [19a, 19d, 27] Comparatively, previous reports[19b, 19c] using Fe₃O₄ as a dehydrogenation catalyst display low yields (1%) at much higher temperatures (345 °C, via thermal heating), suggesting that the required amount of energy for initial activation of Fe₃O₄ can be

achieved at lower bulk temperatures via induction heating. Interestingly, the TMAOH treated sample showed no conversion under induction heating. It was not immediately clear why the TMAOH samples performed worse than the as-synthesized NPs, since they exhibited a higher heating response to magnetic fields (Figure S2), encouraging further surface characterizations. Additionally, commercial NPS (Figure S5), which are agglomerated and randomly shaped, showed 40% smaller aldehyde yield than pyridine treated samples, despite not having bulky ligands on its surface (Figure S6). Uncapped coprecipitated NPs also performed poorly via conventional thermal reactions, indicating that improved yield is not only due to reactant accessibility to the NP surface, but also to enhanced energy transfer via induction heating. Co-precipitated nanoparticles were not tested inductively given their small size (6.6 ± 2.4 nm) places them in the superparamagnetic regime. [26, 28] These results emphasize that although large NPs (commercial), or small and uncapped (co-precipitated) are easier to produce, they cannot outperform the magnetic and catalytic properties achieved via a controlled synthesis. Therefore, further surface characterization studies are needed to determine the surface chemistries of each sample and how the molecular motifs interfere on catalytic activity and heat transfer.

Table 1. Octyl aldehyde yield calculated from GC-FID for various catalysts and control conditions, all performed with the same amount of octanol (1 mL) and duration (6 h).

Type of Passivation	Aldehyde Yield via Thermal Heating (%)	Aldehyde Yield via Induction Heating (%)
As-Synthesized	0.37	0.93
ТМАОН	0.47	0.22
Pyridine	0.61	1.5
Commercial NPs	-	0.62
No Catalyst Control	0.23	-
Co-precipitation NPs	0.24	-

To elucidate the difference in performance between the two phase transfer processes, a series of surface characterizations (TGA, FTIR, neutron scattering, and XPS) were performed. TGA can quantify the extent of the phase transfer since it is known that hydrophilic films can be deposited around colloidal NPs for certain phase transfer agents, such as polydopamine. [29] The TGA results are shown in Table 2 and Figure S7 for the as-synthesized and phase transferred samples. All samples show a slight oxidation to Fe₂O₃ below 250 °C, consistent with partial removal of OA. As expected from the catalysis results, the pyridine treatment decreased the weight loss upon heating to 450 °C (5%), corresponding to a 2.5x decrease in surface ligand density (calculated from TGA weight loss) when compared with assynthesized samples. However, the TMAOH treated sample showed a much larger weight loss (an additional 14%) compared to the as-synthesized, suggesting more TMAOH species are physisorbed after treatment.

Table 2. Weight loss associated to oleic acid from TGA analysis and the respective calculated surfactant coverage compared to BET surface area.

Type of Passivation	· · · · · · · · · · · · · · · · · · ·		BET Surface Area (m²/g)
As- Synthesized	10	3.2	-
ТМАОН	24	9.7	9.6
Pyridine	5	1.1	43.4

The surface areas of the phase transferred samples showed a >4x improvement for the pyridine over the TMAOH treated samples, the former at nearly 65% of the theoretical surface area based on the NP diameter (Table S2). Therefore, pyridine treatment improves OA removal and yields more surface area and available active sites. In contrast, the TMAOH exposure weakens the OA interaction with the surface without removing the ligand, resulting in OA decomposition at high temperatures and low catalytic product conversion for TMAOH treated samples.

To further understand the ligand chemistry on the NP surface, complementary FTIR and INS characterization were employed to identify residual organic groups. Figure 2 shows the offset FTIR spectra of the Fe₃O₄ NPs after the phase transfer treatments. All samples exhibited characteristic methyl C-H vibrations around 2900 cm⁻¹ attributed to OA ligands and TMAOH (when applicable).^[17, 24b, 30] However, the overlap of the C-H (O-H) mode regions corresponding to pyridine and TMAOH limit the identification of the surface species. Nonetheless, vibrational modes at 1255, 1089, and 783 cm⁻¹ appear after the pyridine treatment (arrows in Figure 2), and are attributed to pyridine, which are removed via a methanol wash (green curve in Figure 2).

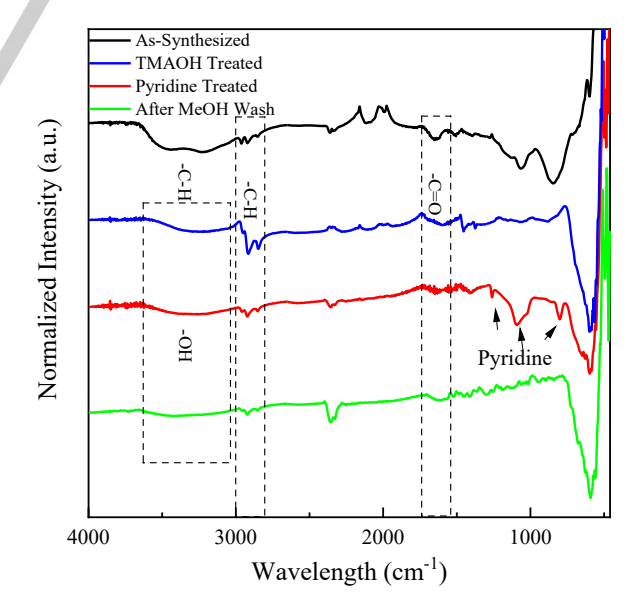


Figure 2. FTIR spectra for as-synthesized and phase transferred samples mixed with KBr at 1:9 ratio (except for as-synthesized). The samples were analyzed on ATR mode, and they show the presence of remaining oleic acid ligands after treatment though the surface is made partially hydrophilic by the presence of hydroxyl groups.

Their easy removal suggests weak physisorption, which is not possible for the strongly bonded OA groups. In an attempt to quantify the ligand coverage and exchange, the ratio of the C-H modes (2900 cm⁻¹) to one for Fe₃O₄ (600 cm⁻¹ Fe-O vibrational mode) were compared.[31] The TMAOH-treated sample shows a higher ratio (0.25) than with the pyridine-treatment (0.10), which can be further decreased to 0.04 after methanol wash, confirming that pyridine exchange lowers the OA ligand density. More importantly, TMAOH significantly alters the C-H/O-H signature at ~3300 cm⁻¹, which is responsible for the hydrophilic nature of the catalysts that allow for dispersion in octanol. However, the FTIR analysis still does not allow for a full picture of the surface-ligand interactions given the spectral overlap and is unable to provide an explanation for the reduced catalytic activity for TMAOH treated samples.[23b] Furthermore, the quantification of the ligand density may be affected by the strong IR absorption of Fe₃O₄, and consequently, chemically specific features of the ligands cannot be identified beyond long akyl chains. For example, a weak C=O mode characteristic of oleic acid at 1700 cm⁻¹ is observed for the as-synthesized samples instead of the traditional sharp peak. [32]

Neutron scattering measurements were performed on the TMAOH treated particles to better understand the bonding structure. In general, OA ligands are expected to dissociate (R-COO¹) during NP growth to bond to the surface. [24, 33] Alternatively, when OA is substituted for oleate ions (NaOL), highly {100} faceted nanocubes are produced. [34] To determine whether residual OA exists in protonated or deprotonated form, INS analysis of the NPs after TMAOH phase transfer is compared to surfactant-free Fe₃O₄ NPs (made by co-precipitation), bulk OA, and a NaOL treated surface (nanocubes). With INS, not only can the ligand be identified with higher specificity than by FTIR, but also the affinity between the native ligand and the displacement agent can be elucidated.

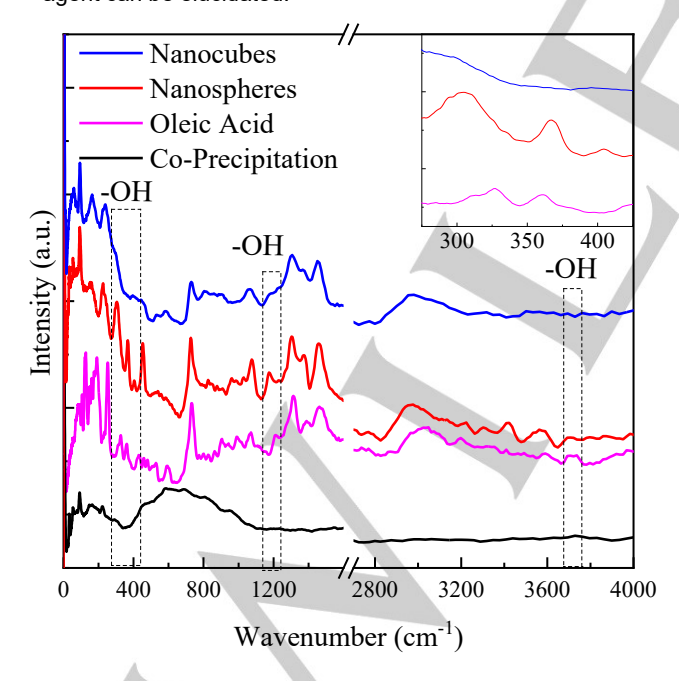


Figure 3. INS spectra for TMAOH phase transferred samples compared to bulk OA. Key vibrational (dashed boxes) modes that involve O-H in the carbonyl group are highlighted to point out their presence on spherical NPs and absence on the cubic NPs. Inset shows a zoomed in image of the vribrational mode at 328 cm⁻¹, shifted due to adsorption.

As expected, the spectra for the TMAOH treated nanospheres and nanocubes are nearly identical to that of the bulk OA sample (Figure 3), emphasizing the inefficiency of TMAOH in removing the native surface ligands. Unlike FTIR spectra, the strong OA signal suggests a high concentration of this ligand on the TMAOH treated NP surface. These high OA concentrations have not been previously identified, likely due to the generation of other hydrophilic groups and their overlap in FTIR vibrational modes with OA, leading to an erroneous assumption of complete ligand removal. [10a, 21b, 22d, 30b] Since the concentration of OA after pyridine treatment decreased by one order of magnitude, INS experiments for these samples could not be performed, given that the OA signal would be below the detection limit for the instrument. Therefore, based on signal intensity alone, it is clear that INS reveals how inefficient the ligand removal is via TMAOH treatment.

A total scattering simulation of the INS spectra for a singlemolecule was performed for OA (in vacuum) and compared to bulk OA (Figure S8) to identify the vibrational modes and the possible binding configurations. The simulated vibrational modes are indexed to the bulk OA and compared to the bonded OA on the NP surface. Although the molecular vibrational modes shift upon adsorption and interparticle interaction^[35], a qualitative identification could be obtained. The analysis of the simulated spectra focused on the terminal hydroxyl group to differentiate between OA and OL binding. The rocking (328, 360 cm⁻¹), scissoring (1211 cm⁻¹), and asymmetric stretching (3756 cm⁻¹) vibrations were used to explore the ligand binding (dashed boxes in Figure 3 and Figure S9). The presence of terminal -OH vibrations is evident on spherical NPs, but not on cubic NPs (Figure 3), suggesting the presence of non-dissociated OA on spherical NPs. More specifically, the vibrational mode at 3756 cm⁻¹ ¹ indicates that OA retains its proton. As anticipated, this mode is not observed in the surfactant-free co-precipitated NPs, demonstrating that the terminal -OH is specific to the OA group and not acquired from ambient moisture. More evidence of nondeprotonation can be drawn from the estimation of the number of hydrogens in a given mode since INS signal intensity increases with total hydrogen cross-section. [36] From the INS peak height, the ratio between the height of the peak at 3756 cm⁻¹ (-OH on the carbonyl group) and 730 cm⁻¹ (hybrid mode involving the backbone of OA) is used to represent the ratio of -OH to the other hydrogens of OA. For nanospheres, this ratio is 0.028 (0.03 for intact OA), while the nanocubes show a negligible peak at 3756 cm⁻¹. These observations suggest that nanospheres treated with TMAOH are surrounded by OA groups that are primarily undissociated and covalently interact with the lattice oxygen (Binding Mode III in Figure 4).

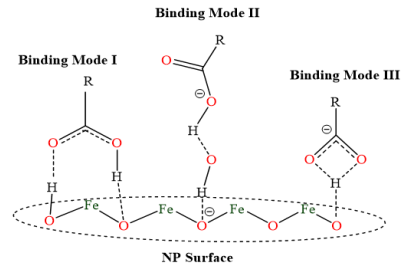


Figure 4. Schematic of the possible binding of OA onto the Fe $_3$ O4 NP surface. Adapted from Deacon and Philips. 64

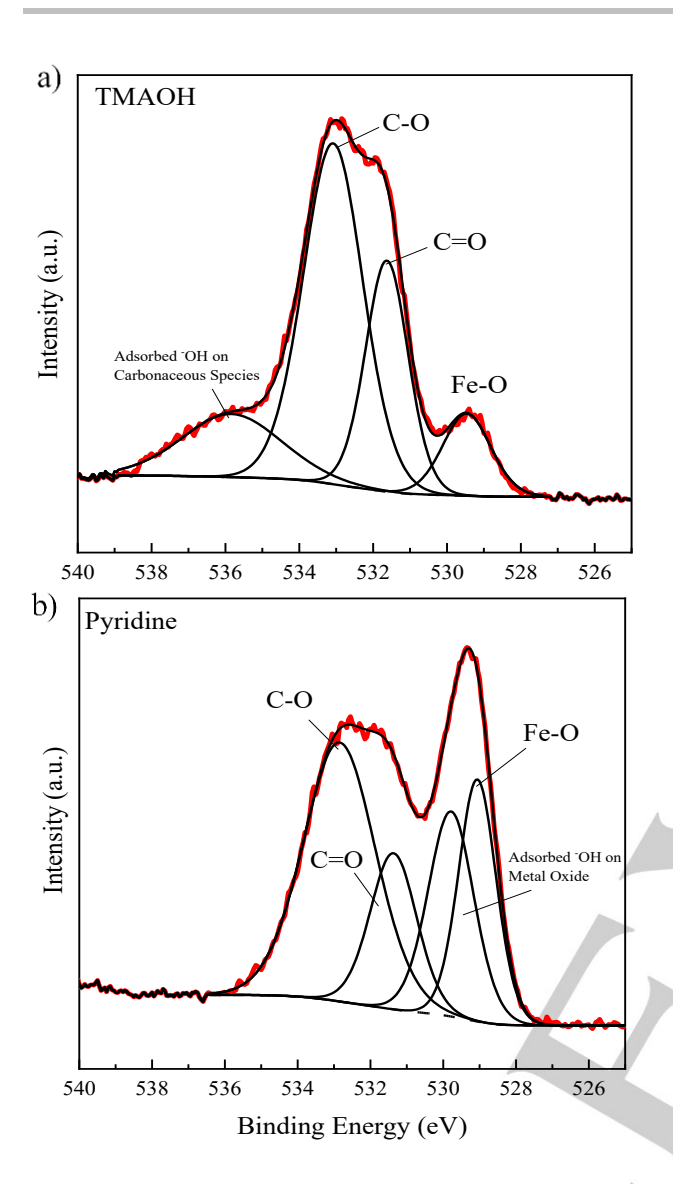


Figure 5. XPS spectra for the O1s of nanospheres treated with TMAOH and pyridine. The C-O bonding composition shown remaining OA ligands on the surface and the shift in OH peak position determines it is located on the NP surface (pyridine) and on the OA layer (TMAOH).

The carboxylate groups on nanospheres can also be coordinated to the metal center in a bidentate form (Structure I in Figure 4)^[37], which constrains the C=O and -OH vibrations, explaining why these are not seen in FTIR but are in INS. In the proposed Binding Mode II, the C=O and -OH vibrations are not constrained and should be visible in FTIR if present. In Binding Mode III, the proton is not released, but interacts directly with a surface oxygen of Fe₃O₄, limiting the effectiveness of the ionic TMAOH to displace the covalently interacting OA. In contrast, pyridine has a lone electron pair with strong affinity to a metal center^[38], and is more likely to displace adsorbed OA.Consequently, the as-synthesized samples are likely represented by Binding Mode I, and, after TMAOH treatment, only a partial recovery of the surface area is possible through rearrangement to Binding Mode III (deduced

from INS). This configuration likely allows for further adsorption of TMAOH species, explaining the increased weight loss and reduced surface area. Additionally, the literature suggests that a secondary OA layer can form around the NP, resulting in other non-dissociated vibrational modes and an IR- active peak for the carbonyl at 1710 cm⁻¹ when excess OA is used. Otherwise, these are absent, demonstrating that the binding modes identified by INS are not due to excess OA.^[39] These proposed binding modes provide insight on the catalytic results, where as-synthesized NPs are in a bidentate mode, which are more robust binding and hinders active sites^[40], resulting in reduced product conversion. In contrast, pyridine treated samples are stronger displacement agents, resulting in a "cleaner" surface for catalysis.

XPS measurements were performed as a final verification of the phase transfer effectiveness in generating a bare catalytic surface. The O 1s spectra for the TMAOH and pyridine treated samples are shown in Figure 5. After peak deconvolution, it can be noted that the relative areas of C-O bonding to Fe₃O₄ are much higher for TMAOH treated samples, confirming the inefficient removal of OA as also seen from the TGA and INS results. Additionally, the adsorbed hydroxyl group peak shifts with surface treatments, from near 531.1 eV^[41] upon pyridine treatment (Figure 5b) to near 535 eV^[42] for TMAOH treatment (Figure 5a). The former is consistent with hydroxylated Fe₃O₄, the latter with organic hydroxyls adsorbed on carbonaceous species, such as in OA. These results also indicate the NP surface is still covered by OA groups after TMAOH treatments. Furthermore, the Fe 2p peak upon pyridine treatment is intense, but there is almost no Fe 2p signal detected from the TMAOH treated sample (Figure S10). The pyridine treated samples also show trace Fe₂O₃ (satellite peak around 718.5 eV)[43], attributed to slight oxidation of the uncapped surface under ambient conditions. However, this oxidation did not affect the induction heating (discussed below) or catalytic results. With respect to the ratio of Fe²⁺/Fe³⁺, a complete quantitative deconvolution is necessary, and while such analyses have been performed by other groups^[44], it is outside of the scope of this work.

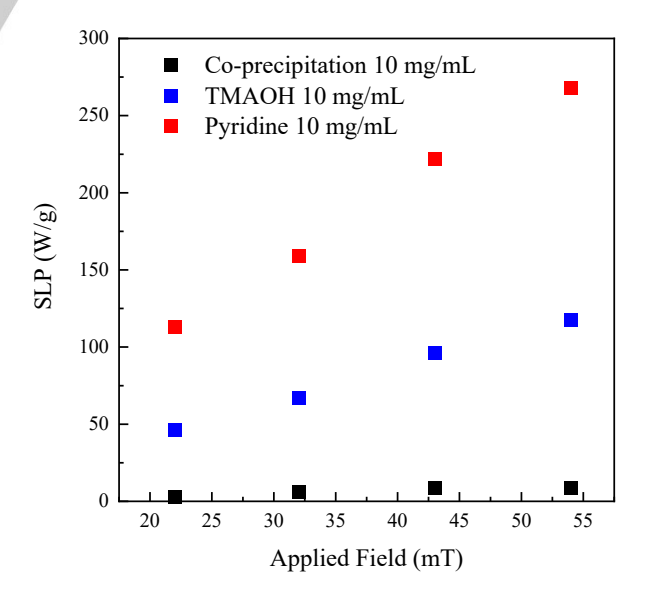


Figure 6. Specific Loss magnet (SLP) for Fe₃O₄ (10 mg/ml) spheres in water with increasing external applied field. Pyridine ligand exchanged particles show higher numbers due to the decreased ligand barrier that can act as heat sinks.

The magnetic hyperthermia (heating) properties of Fe₃O₄ NPs were probed to quantify the effect of ligand removal on the efficiency of heat transfer to the active molecule (octanol). The rate of temperature increase was measured for the spherical NPs treated with TMAOH and pyridine in an aqueous solution (Figure S11) under applied magnetic fields (up to 54 mT). The temperature measurement in solution reflects energy transfer from the NP surface to the aqueous media, since the temperature at the surface of the NP is believed to be much higher (> 30°C) than bulk.[45] Figure 6 shows that the SLP for pyridine ligandexchanged nanospheres is higher than for TMAOH and uncapped (co-precipitation) NPs, at all applied fields. While the magnetic properties of uncapped and capped NPs has already been shown by other groups^[46], this work emphasizes the significant improvement in SLP for particles of nearly the same size and identical shape, by simply treating the surface. Co-precipitated NPs are smaller (6.6 nm) and in a distinct heat generation regime, achieving lower temperatures that are not comparable to colloidal synthesis. The pyridine treatment increases the SLP on average by 2.3x over all applied field, maintaining a linear increase in SLP with the applied field. At higher concentrations, the heating rate drastically changes, increasing the temperature in the media for the same weight of Fe₃O₄ nanoparticles (Figure S11), allowing tunable reaction temperatures. This concentration dependence has also been observed by other research groups.[47] Therefore, with pyridine treated samples, heat transfer to octanol is improved proportional to the increase in heat generation, allowing higher temperatures to be reached at the same applied field.

Conclusion

This work demonstrates a direct relationship between ligand density and heat transfer in induction heating catalysis. Notably, the utilization of TMAOH or pyridine on the surface treatment of Fe₃O₄ plays a crucial role in the induction heating catalysis of 1octanol oxidation. A 2.5x improvement in product conversion for the oxidation of 1-octanol was observed when the nanocatalyst was treated with pyridine to remove surface ligands and increase surface area. Additionally, a 2.5x decrease in ligand density resulted in equivalent heat generation improvement for the same sample. While FTIR characterization suggested low OA surface coverages given the weak signal intensity, INS revealed high concentrations on TMAOH-treated samples. This was further confirmed via XPS, which showed a range of C 1s signatures and a reduced Fe 2p signal intensity. For pyridine-treated samples, the OA displacement improved surface areas by a factor of 4.5 enabling improved oxidation of 1-octanol via induction heating. The reactant's proximity to the heat source, also acting as a catalyst, enabled fast heat transfer to reactants and higher conversion to aldehydes compared to thermally driven reactions. Therefore, the SLP improvement is attributed to a diminished insulating layer of ligands that previously acted as a heat sink and hindered the transfer of heat from the NP surface to the liquid media. The ability to successfully remove the ligand is vital to other catalytic reactions where direct transport of heat to noble metals is necessary to control the conversion and selectivity of a reaction and is the next step in improving energy efficiency in induction heating catalysis.

Experimental Section

Chemicals

1-Octanol (99%, anhydrous, Acros Organics), 1-octene (>99%, TCI), 1-octadecene (90% technical grade, Alfa Aesar), reagent alcohol (94-96%, ACS grade ethanol + methanol, VWR), acetone (99.5%, VWR), dibenzyl ether (98%, Alfa Aesar), n-tetracosane (99%, Alfa Aesar), toluene (99.5%, VWR), hexane (98.5% ACS grade, VWR), iron (III) chloride hexahydrate 99% (FeCl₃.6H₂O, Acros Organics), isopropyl alcohol (99.5% ACS grade, VWR), methanol (99.8% ACS grade, VWR), oleic acid (90% technical grade, Alfa Aesar), pyridine (99.8% anhydrous, Honeywell), sodium oleate (> 97.0%, TCI), and tetramethylammonium hydroxide (25 wt% solution in methanol, BTC) were all used without further purification.

Nanoparticle Synthesis

The synthesis of Fe₃O₄ nanospheres (~18 nm) and nanocubes (~13 nm) was performed according to procedures described elsewhere. [11b],[34a] Nanocubes were used solely as a control sample where the OA is found on its undissociated form, allowing ligand identification through INS. Briefly, an iron oleate (FeOL) precursor is prepared as described in reference 19, washed three times with 100 mL of distilled water, and dried overnight at 110 °C. The resultant dry metal oleate complex is used immediately to prevent oleate polymerization and aging.[40, 48] For nanospheres, 5 mmol of the FeOL was mixed with 13 mmol of OA and 15 mL of a 1:2 v/v benzyl ether:1-octadecene in a 250 mL three-neck round bottom flask. The precursor was degassed at 90 °C for 30 min and heated to 325 °C (3.3 °C/min ramp) under nitrogen atmosphere for 30 min. Similarly, the nanocubes were synthesized by replacing the OA surfactant with sodium oleate (NaOL) at a 1:1 molar FeOL:NaOL ratio in 2:1 w/w mixture of octadecene:n-tetracosane (TCE).[34a] The solution was degassed at 120 °C and refluxed at 337 °C. [34a] The NPs were precipitated with acetone and washed until the supernatant was clear in a 1:4 v/v toluene:acetone solution. As a surfactant-free standard, co-precipitated NPs were also synthesized (see Supporting Information).

Phase Transfer

The hydrophilic NPs were obtained by mixing 3 mL of NP suspension (~3-5 mg/mL, in hexane) with 3 mL of TMAOH and 10 mL of methanol and sonicated for 30 min. The particles were magnetically separated from the solution and washed five times with a 1:4 v/v water:methanol solution to remove the excess TMAOH.^[17] Alternatively, the particle suspension was degassed to remove all hexane, resuspended in an equal volume of pyridine^[49], and stirred overnight at 50 °C. The particles were then precipitated with hexane and subsequently washed four times with isopropanol (IPA) at a 1:4 v/v hexane suspension:IPA ratio. Finally, the precipitate was dispersed in water or methanol and dried under vacuum at 115 °C for 90 min. It is important to remove excess water to decrease the drying time and reduce particle oxidation.^[22a]]

Catalytic Reactions

After surface treatment, spherical NPs were used to probe the induction heating properties of Fe $_3$ O4 under an alternating magnetic field. For thermal and induction heating reactions, the conditions were the same. In a 4-mL ampule, 1 mL of 1-octanol was mixed with 50 mg of the fresh catalyst. For the induction heating reaction, the magnetic field is calibrated such that the temperature in the thermal and the induction heating reactions are the same. Literature shows that once magnetic particles are placed in an alternating magnetic field, their surface temperature is higher than the measured bulk temperature. [45] Given that the 1-octanol boiling point is 195 °C, the solution should boil if a temperature of ~ 200 °C is achieved. For this experimental set-up, boiling was observed when the

bulk temperature measurement was 170 °C, necessitating a thermal reaction temperature of 200 °C for equivalent conditions. Consequently, to account for variations between catalyst syntheses, before each induction heating reaction, the field was set to achieve solvent boiling and a bulk liquid temperature of ~170 °C (Figure S1). The ampule was then sealed in air and placed in an oven (for thermal reaction) at 200 °C or in a three-turn coil at the calibrated field of 343 kHz, for 6 hr (Figure S2). After the catalytic reaction, Fe₃O₄ was separated from the product magnetically, and the liquid was analyzed via Gas-Chromatography using a Flame Ionization Detector (GC-FID). The column used for separation was an Agilent DB-1 (15m x 530 μ m x 1.5 μ m), and a split-flow of 15:1 with He as the carrier gas.

Nanoparticle Characterization

The NP phase was confirmed by X-ray diffraction (XRD) using a PANalytical X-ray diffractometer, operating at 45 kV and 40 mA, with a Cu $K\alpha_1$ (λ = 1.54 Å) as a radiation source. The θ -2 θ radial scan was performed over the range 20-70° with a step size of 0.04° and a dwell time of 60 s. The NP size and shape were characterized by transmission electron microscopy (TEM) using a JEOL JEM-1400 operating at 120 kV, and using an Orius Camera SC1000A 1, with a 0.20 nm lattice image resolution and 0.38 nm point image resolution. The surface ligands were characterized using Attenuated Total Reflectance Fourier-Transform Infrared Spectroscopy (ATR-FTIR), where samples were mixed at 1:9 (w/w) with KBr. X-ray Photoelectron Spectroscopy (XPS) was performed to determine the surface changes (e.g., oxidation) after phase transfer. The spectra were collected for O 1s and Fe 2p in the surface-treated nanospheres using a Scienta Omicron ESCA 2SR XPS system equipped with a monochromatic Al K α (hv = 1486.6 eV) X-ray source and a hemispherical analyzer with a 128-channel detector. The inherent Gaussian width of the photon source was 0.2 eV and the pressure inside the chamber was 1.5×10^{-9} Torr. The XPS spectra were calibrated to the adventitious C 1s peak at 284.6 eV. All peaks were fit (using CasaXPS software32) to symmetric Voigt functions (70% Gaussian and 30% Lorentzian) and a Shirley background to determine peak positions and areas. The fitting parameters were generated with a Levenberg-Marquardt optimization algorithm.

Additionally, nitrogen physisorption measurements were performed using a Micromeritics Gemini VII 2390 Surface Area Analyzer at -196 °C to quantify the active surface area. Thermal Gravimetric Analysis (TGA) was performed with a TA SDT Q600 DSC-TGA under air to quantify the total organic mass. The initial temperature was set to 50 °C and ramped to 500 °C at 10 °C/min. Surface coverages were calculated based on the estimated NP surface area from TEM, and the TGA weight loss attributed to OA molecules. The total amount of OA molecules are estimated using Avogadro's number and divided by the total NP surface area.[22d]Lastly, inelastic neutron scattering (INS) spectra were collected at the Spallation Neutron Source (SNS) at Oak Ridge National Lab on beamline 16B (VISION). This characterization enabled the identification of molecular vibrations even for small sample quantities due to the equipment's highflux (~5x10⁷ neutrons/cm²/s) and high resolution (~1.5% of energy transfer). The spectrum of the empty vanadium sample holder was subtracted from that of the NP powders. For each NP powder analysis, the sample holder was filled with inert gas, sealed, and placed in the beamline. The samples were then cooled to 5 K, and data collected for several hours. The analysis of the vibrational modes of the capping ligands was performed by comparing the NP data to that of pure OA, and indexed using single-molecule Density Functional Theory (DFT) simulations performed using Gaussian software with a 6-311G++(d, p) basis set and B3LYP functional for geometry optimization and frequency calculation. To model the INS spectra, the phonon frequencies are extracted from the singlemolecule calculations automatically by the OCLIMAX package. [50] A single molecule calculation agrees well with the experimental data on the peak positions.

Induction Heating Characterization

The Specific Loss Power (SLP) was extracted by measuring the time-dependent temperature change of water with suspended Fe $_3O_4$ (10, 20, and 40 mg/mL). The solutions were placed in a 3-turn coil, 1 in in diameter, under 0-600 A in an Ambrell EASYHEAT 8130LI 10 kW induction heater, at a constant frequency of 343 kHz, yielding magnetic fields up to 60 mT. The SLP was extracted from the region with the highest slope, prior to plateauing, using the following equation:

$$SLP = \left(\frac{c_{p,np} \, m_{np} + c_{p,w} \, m_w}{m_{np}}\right) \frac{\Delta T}{\Delta t}$$
 Equation 1

Where $\Delta T/\Delta t$ is the slope of Temperature change with time, and $C_{p,np}$ m_{np} and $C_{p,m}$ m_w are the products of heat capacity and mass for the NPs and water, respectively.

Acknowledgements

N.S.M. acknowledges the fellowship support from the Louisiana College of Engineering, the Chevron Fellowship Award, the U.S. Department of Energy (DOE) under EPSCOR grant no. DESC0012432 and John Harvey for the development of a pixel measurement tool to obtain nanoparticle size distributions. K.R.B. acknowledges the Louisiana Board of Regents (LEQSF(2016–19)-RD-A-03) for financial support. J.A.D., C.R., and K.M.D would also like to acknowledge the National Science Foundation, Chemical, Biological, Environmental, and Transport systems for funding under grant no. CBET-1805785. This research used resources at the Spallation Neutron Source, a DOE Office of Science User Facility operated by the Oak Ridge National Laboratory. The authors thank Mr. Tochukwu Ofoegbuna for his assistance in performing XRD characterization.

Keywords: carboxylate ligands • colloidal nanoparticles • induction heating • iron oxide • heterogeneous catalysis

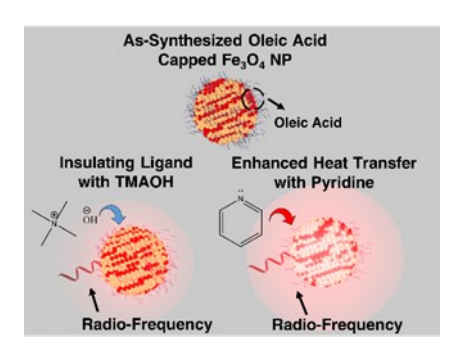
- [1] Brueske, S.; Kramer, C.; Fisher, A. Bandwidth Study on Energy Use and Potential Energy Saving Opportunities in US Pulp and Paper Manufacturing; U.S Department of Energy Advanced Manufacturing Office. 2015.
- U.S. Department of Energy Office of Energy Efficiency & Renewable Energy, Manufacturing Energy and Carbon Footprint-Sector: Chemicals. 2014.
- [3] Koval, C. A.; Lercher, J.; Scott, S. L.; Coates, G. W.; Iglesia, E.; Bullock, R. M.; Jaramillo, T. F.; Flytzani-Stephanopoulos, M.; Resasco, D.; Tway, C. L. Basic Research Needs for Catalysis Science to Transform Energy Technologies: Report from the US Department of Energy, Office of Basic Energy Sciences Workshop 2017.
- [4] a)W. Wang, G. Tuci, C. Duong-Viet, Y. Liu, A. Rossin, L. Luconi, J.-M. Nhut, L. Nguyen-Dinh, C. Pham-Huu, G. Giambastiani, ACS Catal. 2019, 9, 7921-7935; b)K. Aasberg-Petersen, J. H. Bak Hansen, T. S. Christensen, I. Dybkjaer, P. S. Christensen, C. Stub Nielsen, S. E. L. Winter Madsen, J. R. Rostrup-Nielsen, Appl Catal A-Gen 2001, 221, 379-387.
- a)M. Nüchter, B. Ondruschka, W. Bonrath, A. Gum, Green Chem.
 2004, 6, 128-141; b)P. Lisk, E. Bonnot, M. T. Rahman, R. Pollard,
 R. Bowman, V. Degirmenci, E. V. Rebrov, Chem. Eng. J. 2016,
 306, 352-361; c)A. Kirschning, L. Kupracz, J. Hartwig, Chem. Lett.

	2012 , <i>41</i> , 562-570; d)A. Meffre, B. Mehdaoui, V. Connord, J. Carrey, P. F. Fazzini, S. Lachaize, M. Respaud, B. Chaudret, <i>Nano Lett.</i> 2015 , <i>15</i> , 3241-3248.	[22]	a)J. Tang, M. Myers, K. A. Bosnick, L. E. Brus, <i>J. Phys. Chem. C</i> 2003 , <i>107</i> , 7501-7506; b)N. J. Turro, P. H. Lakshminarasimhan, S. Jockusch, S. P. O'Brien, S. G. Grancharov, F. X. Redl, <i>Nano Lett</i> .
[6]	D. Boone, J. Cresko, D. Curry, R. De Saro, M. Glasser, L. Muck, S. Nimbalkar, B. Orthwein, W. Pasley, E. Perez, P. Sheaffer, P. Stephens, U.S Department of Energy - Energy Efficiency & Renewable Energy, 2015 .		2002 , <i>2</i> , 325-328; c)D. V. Talapin, JS. Lee, M. V. Kovalenko, E. V. Shevchenko, <i>Chem. Rev.</i> 2010 , <i>110</i> , 389-458; d)K. Davis, B. Qi, M. Witmer, C. L. Kitchens, B. A. Powell, O. T. Mefford, <i>Langmuir</i> 2014 , <i>30</i> , 10918-10925; e)Y. Wang, J. F. Wong, X.
[7]	a)P. M. Mortensen, J. S. Engbæk, S. B. Vendelbo, M. F. Hansen, M. Østberg, <i>Ind. Eng. Chem. Res.</i> 2017 , <i>56</i> , 14006-14013; b)G. Giambastiani, W. Wang, C. Duong-Viet, G. Tuci, Y. Liu, A. Rossin, L. Luconi, JM. Nhut, L. Nguyen-Dinh, C. Pham-Huu,	[23]	Teng, X. Z. Lin, H. Yang, Nano Lett. 2003, 3, 1555-1559. a)NIST Center for Neutron Research, Neutron scattering lengths and cross sections, Web, https://www.ncnr.nist.gov/resources/nlengths/ 2013; b)B. S. Hudson, J. Phys. Chem. A 2001, 105, 3949-
[8]	ChemSusChem, 2020, 13, 5468. a)C. L. Dennis, R. Ivkov, Int. J. Hyperther. 2013, 29, 715-729; b) E. Wetterskog, CW. Tai, J. Grins, L. Bergström, G. Salazar-Alvarez, ACS Nano 2013, 7, 7132-7144.		3960; c)R. F. Howe, J. McGregor, S. F. Parker, P. Collier, D. Lennon, <i>Catal. Lett.</i> 2016 , <i>146</i> , 1242-1248; d)A. R. McInroy, D. T. Lundie, J. M. Winfield, C. C. Dudman, P. Jones, S. F. Parker, J. W. Taylor, D. Lennon, <i>Phys. Chem. Chem. Phys.</i> 2005 , <i>7</i> , 3093-3101;
[9]	a)Z. Nemati, J. Alonso, L. M. Martinez, H. Khurshid, E. Garaio, J. A. Garcia, M. H. Phan, H. Srikanth, <i>J. Phys. Chem. C</i> 2016 , <i>120</i> , 8370-8379; b)A. Espinosa, R. Di Corato, J. Kolosnjaj-Tabi, P.		e)N. G. Hamilton, R. Warringham, I. P. Silverwood, J. Kapitán, L. Hecht, P. B. Webb, R. P. Tooze, W. Zhou, C. D. Frost, S. F. Parker, D. Lennon, <i>J. Catal.</i> 2014 , <i>312</i> , 221-231.
[10]	Flaud, T. Pellegrino, C. Wilhelm, <i>ACS Nano</i> 2016 , <i>10</i> , 2436-2446. a)J. Xie, C. Xu, N. Kohler, Y. Hou, S. Sun, <i>Adv. Mater.</i> 2007 , <i>19</i> , 3163-3166; b)Lh. Shen, Jf. Bao, D. Wang, Yx. Wang, Zw.	[24]	a)J. Cai, Y. Q. Miao, B. Z. Yu, P. Ma, L. Li, H. M. Fan, <i>Langmuir</i> 2017 , 33, 1662-1669; b)M. Bloemen, W. Brullot, T. T. Luong, N. Geukens, A. Gils, T. Verbiest, <i>J Nanopart Res</i> 2012 , <i>14</i> , 1100.
	Chen, L. Ren, X. Zhou, Xb. Ke, M. Chen, Aq. Yang, <i>Nanoscale</i> 2013 , <i>5</i> , 2133-2141; c)N. Griffete, J. Fresnais, A. Espinosa, D. Taverna, C. Wilhelm, C. Ménager, <i>ACS Appl. Nano Mater</i> 2018 , <i>1</i> ,	[25] [26]	G. D. Gatta, I. Kantor, T. Boffa Ballaran, L. Dubrovinsky, C. McCammon, <i>Phys Chem Miner.</i> 2007 , <i>34</i> , 627-635. S. Tong, C. A. Quinto, L. Zhang, P. Mohindra, G. Bao, <i>ACS Nano</i>
[11]	547-555. a)R. Chen, M. G. Christiansen, P. Anikeeva, <i>ACS Nano</i> 2013 , 7, 8990-9000; b)R. Chen, M. G. Christiansen, A. Sourakov, A. Mohr,	[27]	2017, <i>11</i>, 6808-6816.B. Sarmah, B. Satpati, R. Srivastava, <i>ACS omega</i> 2018, <i>3</i>, 7944-7954.
[12]	Y. Matsumoto, S. Okada, A. Jasanoff, P. Anikeeva, <i>Nano Lett.</i> 2016 , <i>16</i> , 1345-1351. a)W. Wu, E. V. Shevchenko, <i>J. Nanoparticle Res</i> 2018 , <i>20</i> , 255;	[28] [29]	 K. D. Bakoglidis, K. Simeonidis, D. Sakellari, G. Stefanou, M. Angelakeris, <i>IEEE Trans. Magn.</i> 2012, 48, 1320-1323. M. Salomäki, T. Ouvinen, L. Marttila, H. Kivelä, J. Leiro, E. Mäkilä,
	b)L. Xu, J. Wang, <i>Environ. Sci. Technol</i> 2012 , <i>46</i> , 10145-10153; c)Z. Niu, Y. Li, <i>Chem. Mater</i> 2014 , <i>26</i> , 72-83.	[30]	J. Lukkari, <i>J. Phys. Chem. B</i> 2019 , <i>123</i> , 2513-2524. a)R. M. Patil, P. B. Shete, N. D. Thorat, S. V. Otari, K. C. Barick, A.
[13] [14]	ZQ. Wang, ZN. Xu, SY. Peng, MJ. Zhang, G. Lu, QS. Chen, Y. Chen, GC. Guo, ACS Catal. 2015, 5, 4255-4259. M. Siemer, G. Tomaschun, T. Klüner, P. Christopher, K. Al-		Prasad, R. S. Ningthoujam, B. M. Tiwale, S. H. Pawar, <i>RSC Adv.</i> 2014 , <i>4</i> , 4515-4522; b)A. Lak, J. Dieckhoff, F. Ludwig, J. M. Scholtyssek, O. Goldmann, H. Lünsdorf, D. Eberbeck, A.
[15]	Shamery, ACS Appl. Mater. Interfaces 2020, 12, 24, 27765–27776. S. H. Gage, B. D. Stein, L. Z. Nikoshvili, V. G. Matveeva, M. G.	[31]	Kornowski, M. Kraken, F. Litterst, <i>Nanoscale</i> 2013 , <i>5</i> , 11447-11455. S. Mondini, C. Drago, A. M. Ferretti, A. Puglisi, A. Ponti,
	Sulman, E. M. Sulman, D. G. Morgan, E. Y. Yuzik-Klimova, W. E. Mahmoud, L. M. Bronstein, <i>Langmuir</i> 2013 , <i>29</i> , 466-473.	[32]	Nanotechnology 2013 , 24, 105702. L. Zhang, R. He, HC. Gu, <i>Appl. Surf. Sci.</i> 2006 , 253, 2611-2617.
[16]	a)D. Li, C. Wang, D. Tripkovic, S. Sun, N. M. Markovic, V. R. Stamenkovic, ACS Catal. 2012, 2, 1358-1362; b)N. Pinna, S. Grancharov, P. Beato, P. Bonville, M. Antonietti, M. Niederberger, Chem. Mater 2005, 17, 3044-3049.	[33] [34]	 B. Fritzinger, R. K. Capek, K. Lambert, J. C. Martins, Z. Hens, J. Am. Chem. Soc. 2010, 132, 10195-10201. a)M. V. Kovalenko, M. I. Bodnarchuk, R. T. Lechner, G. Hesser, F. Schäffler, W. Heiss, J. Am. Chem. Soc. 2007, 129, 6352-6353; bZ.
[17]	V. Salgueiriño-Maceira, L. M. Liz-Marzán, M. Farle, <i>Langmuir</i> 2004 , <i>20</i> , 6946-6950. a)N. T. N. Truong, W. K. Kim, U. Farva, X. D. Luo, C. Park,	[25]	Zhou, X. Zhu, D. Wu, Q. Chen, D. Huang, C. Sun, J. Xin, K. Ni, J. Gao, <i>Chem. Mater</i> 2015 , <i>27</i> , 3505-3515.
[18]	Sol. Energy Mater Sol. Cells 2011 , 95, 3009-3014; b)H. Skaff, T. Emrick, ChemComm 2003 , 52-53; c)l. Lokteva, N. Radychev, F.	[35]	A. Paulheim, C. Marquardt, M. Sokolowski, M. Hochheim, T. Bredow, H. Aldahhak, E. Rauls, W. G. Schmidt, <i>Phys. Chem. Chem. Phys.</i> 2016 , <i>18</i> , 32891-32902.
	Witt, H. Borchert, J. Parisi, J. Kolny-Olesiak, <i>The J. Phys. Chem. C</i> 2010 , <i>114</i> , 12784-12791; d)JF. Lin, GY. Tu, CC. Ho, CY. Chang, WC. Yen, SH. Hsu, YF. Chen, WF. Su, <i>ACS Appl.</i>	[36] [37]	 K. Gong, Y. Cheng, L. L. Daemen, C. E. White, Phys. Chem. Chem. Phys. 2019, 21, 10277-10292. G. B. Deacon, R. J. Phillips, Coord. Chem. Rev. 1980, 33, 227-
[19]	Mater. Interfaces 2013, 5, 1009-1016. a)M. S. Ahmed, D. S. Mannel, T. W. Root, S. S. Stahl, Org	[38]	250. a)S. Choi, J. Moon, H. Cho, BH. Kwon, N. S. Cho, H. Lee, <i>J.</i>
	Process Res Dev 2017, 21, 1388-1393; b)H. Grabowska, R. Klimkiewicz, L. Syper, J. Wrzyszcz, Top. Catal. 2000, 11, 289-292; c)J. Wrzyszcz, H. Grabowska, R. Klimkiewicz, L. Syper, Catal. Lett. 1998, 54, 55-58; d)T. Ishida, Y. Ogihara, H. Ohashi, T. Akita,	[39]	Mater. Chem C 2019, 7, 3429-3435; b)T. Hanrath, D. Veldman, J. J. Choi, C. G. Christova, M. M. Wienk, R. A. Janssen, ACS Appl. Mater. Interfaces 2009, 1, 244-250. a)K. Yang, H. Peng, Y. Wen, N. Li, Appl. Surf. Sci. 2010, 256,
[20]	 T. Honma, H. Oji, M. Haruta, <i>ChemSusChem</i> 2012, 5, 2243-2248. P. Guardia, N. Pérez, A. Labarta, X. Batlle, <i>Langmuir</i> 2010, 26, 5843-5847. 		3093-3097; b)R. A. Harris, P. M. Shumbula, H. van der Walt, <i>Langmuir</i> 2015 , <i>31</i> , 3934-3943; c)Q. Lan, C. Liu, F. Yang, S. Liu, J. Xu, D. Sun, <i>J. Colloid Interface Sci.</i> 2007 , <i>310</i> , 260-269.
[21]	a)K. E. Sapsford, W. R. Algar, L. Berti, K. B. Gemmill, B. J. Casey, E. Oh, M. H. Stewart, I. L. Medintz, <i>Chem. Rev.</i> 2013 , <i>113</i> , 1904-	[40]	L. M. Bronstein, X. Huang, J. Retrum, A. Schmucker, M. Pink, B. D. Stein, B. Dragnea, <i>Chem. Mater</i> 2007 , <i>19</i> , 3624-3632.
	2074; b)A. Dong, X. Ye, J. Chen, Y. Kang, T. Gordon, J. M. Kikkawa, C. B. Murray, <i>J. Am. Chem. Soc.</i> 2011 , <i>133</i> , 998-1006; c)M. Green, <i>J. Mater. Chem</i> 2010 , <i>20</i> , 5797-5809.	[41] [42]	 JC. Dupin, D. Gonbeau, P. Vinatier, A. Levasseur, Phys. Chem. Chem. Phys. 2000, 2, 1319-1324. M. Li, C. Bian, G. Yang, X. Qiang, Chem. Eng. J. 2019, 368, 350-

- [43] Y. V. Kolen'ko, M. Bañobre-López, C. Rodríguez-Abreu, E. Carbó-Argibay, A. Sailsman, Y. Piñeiro-Redondo, M. F. Cerqueira, D. Y. Petrovykh, K. Kovnir, O. I. Lebedev, J. Rivas, J. Phys. Chem. C 2014, 118, 8691-8701.
- [44] B. Lesiak, N. Rangam, P. Jiricek, I. Gordeev, J. Tóth, L. Kövér, M. Mohai, P. Borowicz, Front Chem 2019, 7.
- [45] A. Riedinger, P. Guardia, A. Curcio, M. A. Garcia, R. Cingolani, L. Manna, T. Pellegrino, Nano Lett. 2013, 13, 2399-2406.
- [46] S. Gyergyek, D. Makovec, M. Jagodič, M. Drofenik, K. Schenk, O. Jordan, J. Kovač, G. Dražič, H. Hofmann, J. Alloys Compd. 2017, 694, 261-271.
- [47] a)A. S. Eggeman, S. A. Majetich, D. Farrell, Q. A. Pankhurst, *IEEE Trans. Magn.* 2007, 43, 2451-2453; b)H. Xu, Y. Pan, *Nanomaterials* 2019, 9, 1457.
- [48] a)J. Lynch, J. Zhuang, T. Wang, D. LaMontagne, H. Wu, Y. C.
 Cao, J. Am. Chem. Soc. 2011, 133, 12664-12674; b)A. P. Herrera,
 L. Polo-Corrales, E. Chavez, J. Cabarcas-Bolivar, O. N. C.
 Uwakweh, C. Rinaldi, J. Magn. Magn. Mater. 2013, 328, 41-52.
- [49] D. H. Webber, R. L. Brutchey, J. Am. Chem. Soc. 2012, 134, 1085-1092
- [50] Y. Cheng, L. Daemen, A. Kolesnikov, A. Ramirez-Cuesta, J. Chem. Theory Comput. 2019, 15, 1974-1982.



Entry for the Table of Contents



Scheme 1: Illustration of the effect of ligand removal on heat transfer when a magnetic NP is activated with an alternating magnetic field using Radio-Frequency. While TMAOH treatment resulted in higher surface ligand density, acting as heat sink, pyridine treatment reduced ligand density and improved the extent of heat transfer.

